

A review of high nanoparticles concentration composites: semiconductor and high refractive index materials

Igor Yu. Denisyuk

*Doctor of Science, professor, head of the chair of Quantum Sized Optical Systems of State University of Information Technologies, Mechanics and Optics
Russia, 197101, Saint-Petersburg, Str. Kronverskii 49*

Mari Iv. Fokina

*Assistant professor of State University of Information Technologies, Mechanics and Optics
Russia, 197101, Saint-Petersburg, Str. Kronverskii 49*

1. Introduction

At the present time homogeneous optical and optoelectronic media such as glasses, monocrystals and polymer materials are widely used. Each of these media has a specific set of properties. For example, the polymer materials allow producing flexible and transparent films, for example film OLED. They are cheap. The technology of polymers treatment is very simple and suitable for some applications. However the holes and electrons mobility in polymer materials are many time less in comparison with inorganic well known semiconductors. Another problem is a relative high exciton decay energy in polymer with value of 100 meV that result on temperature dependence of photogeneration.

The possibility of combining the different properties into a single material should be rather useful. It is impossible to solve this problem by traditional ways because the properties reflect the internal structures of these different materials.

The method of nanostructuring provides the possibility of combining the properties of polymers and crystals. The resulting nanocomposite is the mechanical mixture of inorganic semiconductor distributed uniformly in the polymer matrix. Under the condition of uniform distribution of nanoparticles and if the size of such nanocrystals is small (2-5 nm), they don't distort an incident light wave and the light scattering is low. If to use high refractive index nanoparticles such as ZnS, CdS, ZnO, TiO₂ incorporation of nanoparticles into polymer will result on significant increasing of refractive index of material. Same time these material has a proprieties of homogenous semiconductor material because of small nanometer size distance between semiconductor nanoparticles and easy tunnel transportation of charge carrier. Nanocomposite with high concentration of small size nanocrystals becomes effectively a homogeneous medium, having semiconductor proprieties of inorganic material with low scattering and good flexibility and processability of polymer. The set of properties of this mixture is determined by both components, namely polymer and nanocrystals, and

by the ratio of concentrations of them. The main efforts of research directed to develop quasi-homogeneous nanocomposite material with nanoparticles and polymer matrix comparable content for photonics application areas: photoresist for nanolithography, microoptics, organic solar cell and OLED.

2. Crystalline lattice of small nanoparticles

Physics of semiconductor theory use macroscopic charge carrier statistic parameters of bulk crystals for all structures types including microns and sub-microns elements in microchips. It is correct approximation now as the sizes of microchips elements more than 100 nm are more time larger in comparison to interatomic distances. In contrary, typical nanoparticles, for example CdS or ZnS with the size of 1 - 3 nm include a few atomic layers and its interatomic distance can differ essentially from same of bulk crystals. Now are a few of works where these effects are investigated.

Indeed, if to shrink elements down to the nanometer scale, creating nanodots, nanoparticles, nanorods and nanotubes a few tens of atoms across, they've found weird and puzzling behaviors unexpected for bulk and micron sized material.

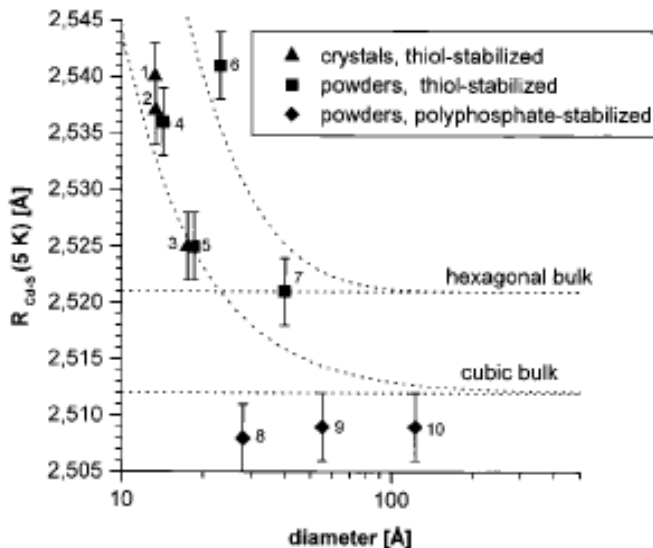


Fig. 1. Mean Cd-S distances R_{Cd-S} as a function of the size of CdS nanocrystals deduced from EXAFS experiments. Bulk values of the cubic and the hexagonal phase of CdS are also indicated (dotted).

Certainly at decreasing of nanoparticles sized up to few nanometers that correspond to some tens atoms its crystalline lattice change essentially from same of bulk crystal and it is appear instability of crystalline lattice. Large surface of small particle will result on augmentation of influence of surface states on crystalline lattice of nanoparticles.

There are a lot of work that show size and surface effects of crystalline lattice change in nanometers size nanoparticles.

In the work [1] it is shown nanoparticles crystalline lattice parameter dependence from organic substance settled on its surface and its size. Micron size particles, for example CdS have crystalline lattice similar to bulk crystals at decreasing of nanoparticles sizes down to nanometers range its lattice change essentially.

In Fig. 1 show Cd-S distance dependence from nanoparticles diameter and organic shell nature.

A few CdS samples have been investigated, the particles differing in size and crystal structure:

- three samples of polyphosphate-stabilized nanoparticles with cubic crystal structure (diameters approximately 3.0-12.0 nm),
- four samples of thioglycerol-stabilized particles (hexagonal and cubic (see below), diameters from 1.4 to 4.0 nm), and
- three samples of crystallized nanoparticles, the structures and superstructures of which are known from SC-XRD (diameters from 1.3 to 1.7 nm).

Microcrystalline CdS of hexagonal crystal structure was used as a reference substance. The smallest "particles" investigated consist of a three-dimensional network of $Cd_8(SR)_{16}$ units (R) thioglycerol), which may serve as a model for the surface of thiol-stabilized CdS nanocrystals. The other two crystallized clusters ($Cd_{17}S_4(SR)_{26}$ and $Cd_{32}S_{14}(SR)_{36}$, R) mercaptoethanol and 1-mercapto-2-propanol, respectively) may be regarded as fragments of the cubic (zinc blende) phase of CdS and appear tetrahedrally. Thus, at least for the latter three samples, "diameter" is to be taken only as a reference point for the "size" of the particles. EXAFS spectra have been taken in transmission mode at the Cd K-edge in the energy range from 26.4 to 29.0 kV at temperatures between 5 and 296 K.

All of the samples clearly showed the Cd-S coordination shell, whereas the Cd-Cd coordination (second shell) was visible in particles larger than 3.0 nm only. Figure 1 shows the dependence of the Cd-S bond length as a function of the particle diameter deduced from the EXAFS analysis. The quality of the data allows us to divide the plot into three regions. Samples 8-10 exhibit a slight contraction of the Cd-S bond with decreasing particle size, which is due to the minimization of the surface energy, obviously unhindered by the ionically bound stabilizers.

In contrast, the covalently bound stabilizers of samples 1-5 expand the Cd-S bond. This expansion is larger for the smaller particles, and it becomes larger as the steric interaction among the stabilizers comes into effect. For samples 1-3, the bond lengths determined by EXAFS match very well those from the SC-XRD analysis. From P-XRD, sample 7 is assigned to the hexagonal crystal phase, by means of which the larger mean bond length, compared to samples 8 and 9 (similar size but cubic phase), is explainable. Like sample 7, sample 6 is prepared at elevated temperatures, which makes it likely that this sample also belongs to the thermodynamically stable hexagonal crystal phase (P-XRD does not allow an unambiguous assignment). This guess is corroborated by the "out of order" bond length (Fig. 1) and by the analysis of the third moments of the pair distribution function (Fig. 1). According to the surface-to-volume ratio of the nanocrystals, this quantity increases with decreasing particle size but is divided into two groups: on one hand, all particles clearly belonging to the cubic structure (four equivalent Cd-S bonds lead to C3) for the largest particles) and on the other hand, samples 6 and 7, with distinctly elevated anharmonicity (in hexagonal CdS, three Cd-S bonds are equivalent, and one differs from those). Thus, for sample 6, we are in a position

to state the assignment to the hexagonal phase by means of EXAFS spectroscopy, which has not previously been possible, by applying P-XRD and HRTEM. The Debye temperatures and static disorders are extractable from the EXAFS data together with the bond lengths and anharmonicities, as mentioned above. The Debye temperatures that were determined increased slightly with decreasing particle size, which points to a stiffening of the Cd-S bonds. When compared to the bulk value, all of the nanoparticles displayed an elevated static disorder, which, in the first instance, increases with decreasing size according to the surface-to-volume ratio (samples 10-6). For the very small clusters of samples 1-5, again slightly reduced static disorders are observed (in good agreement with the SC-XRD of samples 1-3). Possibly, this finding is a hint toward different regimes of particle growth: thermodynamically controlled growth leads to a crystallizable species, whereas subsequent Ostwald ripening yields larger and less specific colloids.

At decreasing of nanoparticles sizes up to 1 nanometers distances in crystalline lattice between metal atoms will increase that result of moving from crystalline to amorphous state of material in result. Transformation from crystalline to amorphous form of small particles well known for Fe_2O_3 , Se, inorganic materials.

3. Methods of preparation and stabilization of semiconductor nanoparticles

3.1 Inorganic nanoparticles based nanocomposit

From 90 years was develop the main methods of nanoparticles synthesis. Few nanoparticles types now is commercial available from Aldrich and other commercial supplier. Methods of the nanoparticles synthesis can be divided into three main groups.

1. Synthesis of semiconductor nanoparticles in solutions of the corresponding salts by controlled addition of anions (or cations) or by hydrolysis [2];
2. Preparation of nanoparticles as a result of phase transformations [3];
3. The synthesis of nanoparticles in aerosols [4].

Preparation of nanocomposite material having both high nanoparticles concentration, absence of its coagulation and homogeneous optical and semiconductor proprieties is a mostly difficult problem. Usually it accomplished by preparation of suitable nanoparticles with modified surface and then to its incorporation in polymer, having surface active proprieties often.

For consideration of nanoparticles state in nanocomposite, we should assume that nanoparticles can interact with polymer matrix with formation of ordered polymer layers in its surface. In the work [5] was made numerical study of state of nanoparticles (fullerene) in polymer matrix and received interesting results on this bi- phase system elastic proprieties.

The purpose of this work is to investigate the effect of nanoparticle size on elastic properties of polymeric nanocomposites using MD simulations. For this, molecular models of a nanocomposite were constructed by reinforcing amorphous polyethylene (PE) matrix with nano sized buckminster fullerene bucky-ball (or simply bucky-ball). Bucky-balls of three different diameters (0.7, 1.2 and 1.7 nm, respectively) were utilized to incorporate size effect in the nanocomposites. To represent them as a generic nanoparticle system, all bucky-balls were configured as rigid body. This is necessary because a bucky-ball embedded inside the polymer matrix may deform excessively depending on its size and may overshadow the composite mechanical properties attributed to filler size. The assumption of rigid bucky-ball will ensure that the shape of filler does not contribute to variation in elastic properties. The

assumption may be unrealistic for large diameter buckyballs, it is a reasonable assumption for small bucky-balls and solid nanoparticles. In addition to this shape constraint, the volume fraction of the filler, matrix characteristics (density, molecular weight, molecular weight distribution, branch content, degree of crystallinity, etc.) and their force interaction with the nanoparticle were kept constant in all nanocomposites. Molecular models of the neat PE matrix were also developed for comparison. Elastic properties of the neat and nanocomposite systems were then evaluated using four different modes of deformation, namely, unidirectional tension and compression, and hydrostatic tension and compression, respectively.

Molecular models of nanocomposites were developed by symmetrically placing a spherical fullerene bucky-ball in the PE matrix, as shown schematically in Fig. 2. The dashed box in Figs. 2 a and b indicates the periodic cell or unit cell that was simulated by MD. Three types of bucky-balls, C60, C180 and C320 (subscripts denote number of carbon atoms), were used to incorporate the size effect. All bucky-balls were infused in matrix by approximately 4.5 vol%. Periodic boundary conditions were employed to replicate the unit cells in three dimensions. In nanocomposites, the PE matrix was represented by united atom (UA) -CH₂-units. The initial structure of the matrix was constructed by positioning the bucky-ball at the center of the unit cell and by randomly generating PE chain(s) on a tetrahedron lattice surrounding the bucky-ball.

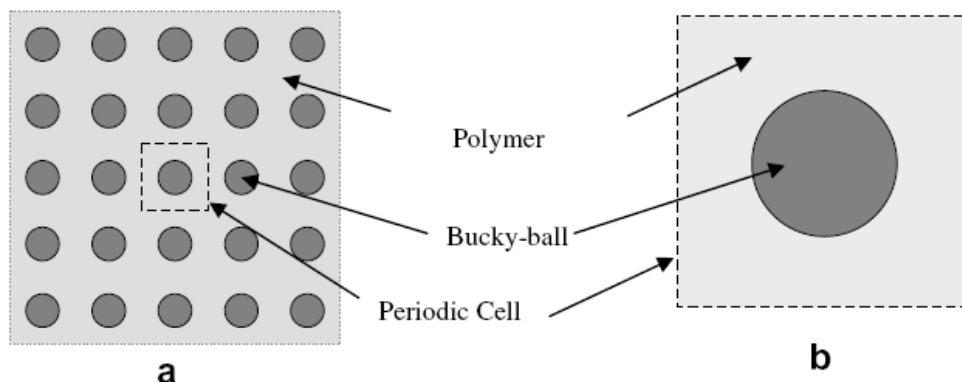


Fig. 2. (a) Schematic diagram of polymer nanocomposites, (b) periodic cells used for MD simulations.

Numerical simulation shown that elastic properties of nanocomposites are improved appreciably with the infusion of bucky-balls in PE matrix. The trend shows that with the increase in filler size, the extent of enhancement in elastic properties is gradually reduced. The result is somewhat surprising because in all cases the volume fraction was maintained constant (4.5%).

It can be concluded from this observation that size of the filler has considerable influence on polymer density even with non-bonded inter-molecular interactions between polymer and nanoparticle. The effect can be well understood from the radial density distribution of PE for both neat and nanocomposites, as shown in Fig. 3 in which the distribution is constructed by measuring local densities of PE at various radial distances starting from the center to the

half-length of the periodic box. It is interesting to find that local densities are not constant along the radial distance. A 200–250% increase in polymer density exists for all nanocomposites at a distance close to the nanoparticle. At further distances, the distribution fluctuates in a similar manner as in the neat polymer system. The fluctuating character is inherent because mass needs to be conserved [6]. The collective contributions of these factors yielded a decreasing trend in polymer bulk density with the increment of filler size. It appears from the analysis that polymer density distribution plays the foremost role in size effect. However, it is not elucidated why size difference influence polymer density. The discernible contribution from filler size can be realized from radial distribution plot as shown in Fig. 4.

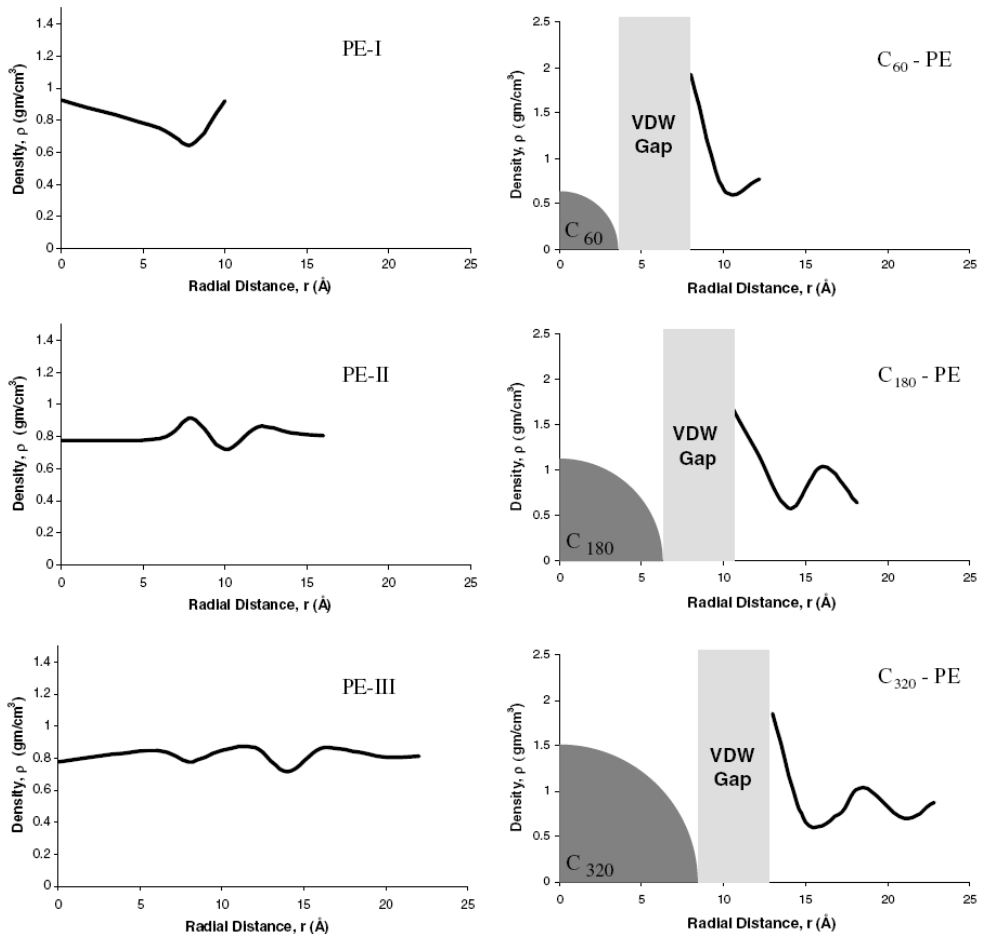


Fig. 3. Radial density distribution of various: (a) neat PE and (b) nanocomposite models. Space occupied by nanoparticles is schematically shown by the quarter circles.

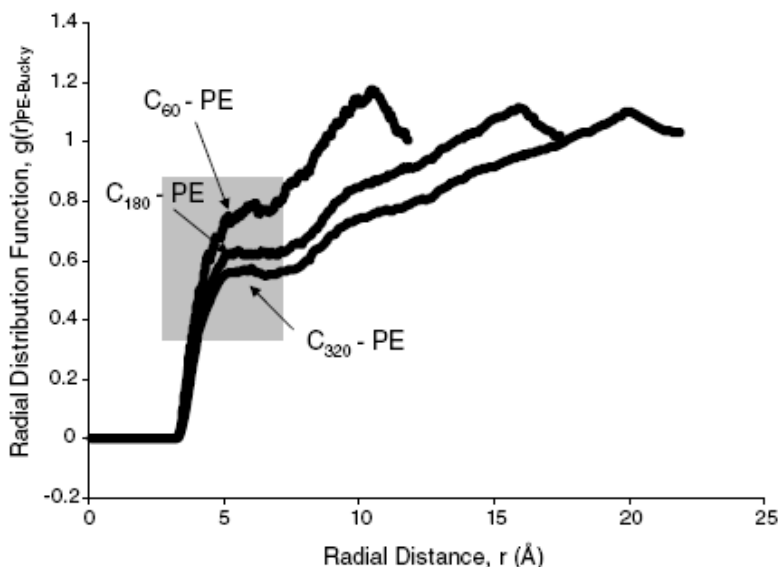


Fig. 4. PE-Bucky radial distribution functions (RDF) of various nanocomposite models.

It is known that the radial distribution function for any atom pairs gives a measure on how corresponding atoms are distributed in three-dimensional space due to VDW interactions. Hence, $g(r)_{PE-Bucky}$ refers to radial distribution of PE atoms with respect to Bucky-ball atoms. As atomic position of all bucky-balls were fixed, a plot of $g(r)_{PE-Bucky}$ would thus provide information about the polymer distribution due to interaction with a nanoparticle. Fig. 4 reveals that the size of Bucky-ball has strong influence on the $g(r)$ plot. It is observed that the value of $g(r)$ assumed zero from 0 to 3.4 Å for all nanocomposites, then increases with radial distance. The zero value refers to the VDW thickness h . It is also evident that h does not depend on filler size. It is quite expected because parameters describing LJ potentials are identical for all nanocomposites and the nature of the h is known to be governed by such interactions between nanoparticle and polymer [7]. However, the relative distribution of polymer atoms towards the nanoparticle, as indicated by the variation in $g(r)$ at a particular radial distance, is quite different with the change in filler size. It is obvious from Fig. 4 that more atoms are tending to disseminate across the polymer-nanoparticle interface as the size of buckyball decreases.

It appears from the above discussion that with the reduction in filler size, the bulk density of polymer and the attractive interaction energy between polymer and nanoparticle at the interface increase substantially. Enhancements of these parameters are then translated to improved elastic moduli.

Preparation of nanocomposite with high nanoparticles content.

According to above numerical simulation and discussion there are strong interaction between polymer and nanoparticles. At rapprochement of nanoparticles up to distance of 3 - 5 nm nanocomposite behavior change dramatically. In real nanocomposite with nanoparticles size of 2-3 nm these condition of nanoparticles - nanoparticle distance about 3 nm begin with about 10 vol. % nanoparticles concentration. So, 10 % is a border between

usual nanocomposite with no nanoparticles interaction and high nanoparticles concentration composite where nanoparticle - nanoparticle interaction play the main role in behavior formation of whole composition.

At preparation of nanocomposite with high nanoparticles concentration a contradiction is appear: to avoid nanoparticles coagulation we need to increase interaction between them and the polymer matrix, but at the same time those interactions with polymer will result in hardening of the composites in result of polymer cross-linking over nanoparticles.

In most part research this contradiction has been avoided by use of very fast drying of material [8]. At fast drying nanoparticles have not enough time for coagulation and solid material keep good distribution take place in solution. In that works, the dangerous stage of particles interactions passed fast and the composites kept their transparency. For example, if a layer is prepared by spin coating, the process of solid coating preparation occupies only some part of a second. Certainly, this method is not suitable for preparing thick nanocomposite layers and bulk nanocomposites.

Next two works show possibility to obtain high nanoparticles concentration in material that suitable to obtain high refractive index homogenous nanocomposite material based on high concentration of ZnS or CdS semiconductor nanocrystals in polymeric matrix. Same homogenous nanocomposite with high semiconductor nanoparticles concentration around 20 - 30 vol % are suitable as a homogenous semiconductor materials, so synthesis of these materials were described in detail here.

One example of high concentration ZnS nanocomposit thin film preparation give the work [8]. In the work was used previously prepared ZnS-monomers prepolymer that was UV-cured at once after spin coating in thin film. UV curing technology was used to rapidly prepolymerize the ZnS-macromer system, and then a radical polymerization process was carried out to complete the polymerization reaction. Another advantage of using this macromer is that the macromer in solution has a viscosity, which is favorable for spin-coating to form films. Furthermore, a polymerizable moiety as capping agent has also been utilized to modify the surface of ZnS nanoparticles in order to immobilize the ZnS particles into the polymer. Research on the preparation of nanoparticles-polymer composites using polymerizable surfactants, ligands or capping agents has previously been reported [9, 10]. This approach can effectively avoid the phase separation and results in transparent composites because the functionalized inorganic particles with polymerizable vinyl groups can be copolymerized with the monomers to form integrated polymeric materials.

In this work firstly was being synthesized the thiophenol (PhSH)-4-thiomethyl styrene (TMSt)-capped ZnS nanoparticles with high concentration in DMF. Then a UV curable urethane-methacrylate macromer (UMM) was introduced into the nano-ZnS containing DMF solution. The ZnS nanoparticles were immobilized into the polymer matrix via copolymerization of the macromer (UMM) with 4-thiomethyl styrene (TMSt) bound on the surface of ZnS particles to synthesize a series of nano-ZnS-poly(urethane-methacrylate macromer) (PUMM) transparent composite films with high refractive indices. The structure and composition of the thiolcapped ZnS nanoparticles were characterized via TEM, X-ray, FTIR and chemical analyses. The thermal properties, optical properties and microstructure of the nanocomposite films were investigated in detail.

Detailed description of high concentration nanocomposite synthesis method according to work [8].

3.2 Materials

Anhydrous zinc acetate, N,N-dimethylformamide (DMF), thiophenol (PhSH), thiourea, 2,4-tolylene diisocyanate (TDI), dibutyltin dilaurate (DBTL), 2-hydroxyethyl methacrylate (HEMA) and other chemical reagents were of analytical grade and were used without further purification. 4-Vinylbenzyl chloride (w 95% GC grade, Fluka) and 2,2-dimethyl-2-hydroxyacetophenone (Darocur 1173 from Ciba Special Chemicals) were used as received. 2,2'-Dimercaptoethyl sulfide (MES) was synthesized as reported previously [11]. Synthesis of 4-thiomethyl styrene (TMSt) TMSt was synthesized from 4-vinylbenzyl chloride in a manner similar to that reported in the literature [12]. 15.3 g of 4-vinylbenzyl chloride (0.1 mol), 9.12 g of thiourea (0.12 mol), 200 ml of ethanol and 0.08 g of p-methoxyphenol as inhibitor were put into a four-necked flask fitted with a reflux condenser. The reaction mixture was stirred at reflux temperature for 4 h under N₂ flow and then was cooled. 75 ml of 20% solution of sodium hydroxide were added to the above mixture, and the resulting solution was immediately heated to 80 C and continuously stirred at 80 C for 0.5 h. Finally, the resulting solution was cooled to room temperature and 100 ml of CHCl₃ were added. The organic phase was separated out and washed with distilled water until neutral. Then the organic phase was dried over anhydrous Na₂SO₄ and the product (TMSt) was obtained by removing the organic solvent under reduced pressure. Yield 75%, n₂₀ d ~ 1.625. The method for preparing thiol-capped ZnS nanoparticles (TCZnS) was similar to that reported in ref. [8].

3.3 Preparation of ZnS–PUMM nanocomposite films

UV curable macromers (UMM)–DMF solution of desired weight ratio, containing 2 wt% of Darocur1173 and 0.5 wt% of AIBN as initiator were mixed with 3 ml of thiol-capped colloidal ZnS–DMF solution according to the required doping content of ZnS particles in the films. The mixture solutions were concentrated to a suitable viscosity at room temperature under vacuum, and the resulting viscous solution was spincoated on silicon wafers or quartz plates at 1000–3000 rpm.

The coated films were dried under vacuum for 10 min at 45 uC, and then were exposed to the UV radiation of a medium pressure mercury lamp of 2 kW for 3 min. After UV curing reaction, the films were cured at 70 uC for 2 h, 100 uC for 1 h, 120 uC for 1 h and treated at 160 uC for 0.5 h.

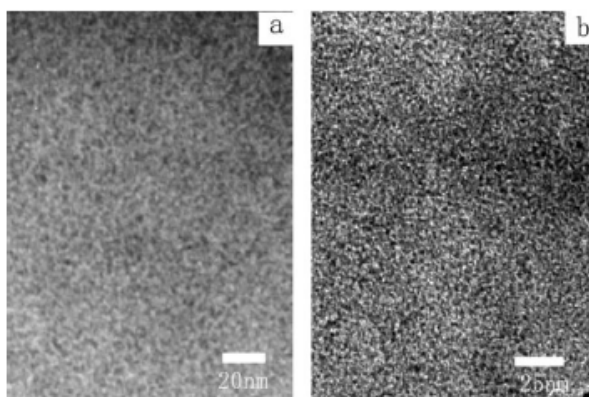


Fig. 5. TEM micrographs of the nanocomposite films of (a) TCZnS32 and (b) TCZnS79.

Resulting TEM micrographs of the nanocomposite films TCZnS32 and TCZnS79 are shown in Fig. 5. The ZnS nanoparticles ranging from 2 to 5 nm are uniformly dispersed inside the polymer matrix and the ZnS nanoparticles remain their original size without aggregation after immobilization into the polymer matrix, indicating that the thiol capping agents and polymer play an important role in stabilizing and dispersing nanoparticles.

The main properties of nanocomposites with different content of ZnS nanoparticles are shown in Table 1.

The WXR pattern of ZnS nanoparticles synthesized in the work shows broad peaks typical of samples in the nanosize regime (Fig. 6). The peaks in the diffraction pattern appearing at 2θ values of 28.5, 47.5 and 56.3° correspond to (111), (220) and (311) planes of the cubic structure of sphalerite ZnS. The resulting ZnS crystallite structure is in accordance with that reported previously.

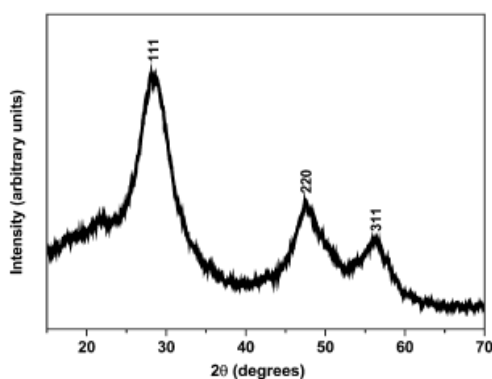


Fig. 6. Wide-angle X-ray diffraction pattern of PhSH-TMSt-capped ZnS nanoparticles.

The FTIR spectrum of the PhSH-TMSt-capped ZnS nanoparticles is shown in Fig. 7.

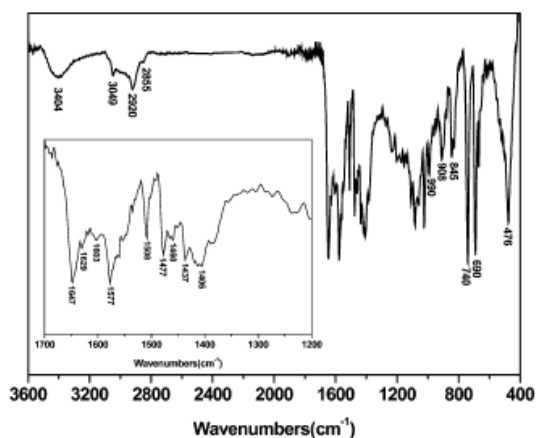


Fig. 7. FTIR spectrum of PhSH-TMSt-capped ZnS nanoparticle powder, dried from colloidal ZnS-DMF solution in vacuum.

The peaks at 2920, 2855 and 1406–1477 cm^{-1} are assigned to the characteristic vibration of the methylene groups in TMSt. The peaks assigned to C–C vibrations of benzene rings are observed at 1603, 1577, 1508 and 690–990 cm^{-1} . The stretching vibration band of vinyl groups on TMSt located at 1629 cm^{-1} also appears in Fig. 7 (insert), although its intensity is very weak. The absorption peak of the S–H vibration at 2550–2565 cm^{-1} is not observed in the IR spectrum, indicating that the mercapto groups of TMSt and PhSH molecules were bound to the ZnS nanoparticle surface. The band of the C=O stretching vibration on residual DMF molecules is also observed at 1647 cm^{-1} which is lower than that of free DMF molecules at 1667 cm^{-1} . This shift reflects that there is a relatively strong interaction between DMF molecules and the surface of colloidal ZnS nanoparticles.²⁸ In addition, the broad peak near 3404 cm^{-1} in the IR spectrum may be from the absorption of traces of moisture or adsorbed water associated with DMF.

The chemical composition of the thiol-capped ZnS nanoparticles was determined by EA and ICP-AES analyses. Anal. Found: C, 30.5; H, 2.66; S, 25.30; Zn, 42.90. The relative molar ratio of S to Zn was calculated to be 1.2 on the basis of the above quantitative analyses. This result is in good accordance with the EDAX result for ZnS particles, which showed that the ratio of the number of S to that of Zn is 1.18 within an accuracy of 2%. If all of the capping agents (RSH) are capped on the ZnS particles, the molar ratio of $\text{Zn}^{2+} : \text{S}^{2-} : \text{RS}^-$ was calculated to be 1 : 0.6 : 0.6, based on the feed ratio ($\text{Zn}^{2+} : \text{RSH} \sim 1 : 0.6$), and the contents of carbon and hydrogen on the ZnS particles were also calculated to be 31.8 and 2.78, respectively. The contents of these two elements agree well with the results of chemical analyses (EA and ICP-AES) within experimental error. Therefore, it can be deduced that almost all of the capping agents, PhSH and TMSt, were capped to the ZnS particles and the molar ratio of $\text{Zn}^{2+} : \text{S}^{2-} : \text{RS}^-$ for the PhSH–TMSt-capped ZnS particles was determined to be 1 : 0.6 : 0.6.

3.4 Nanocomposite films

FTIR spectra of the ZnS–PUMM nanocomposite films for the TCZnS16–TCZnS79 are shown in Fig. 8 (X is weight percent of PhSH–TMSt-capped ZnS particles in the films). The absorption peaks at 3300 and 1657 cm^{-1} are attributed to N–H and C=O bonds of urethane linkages and the latter covers the characteristic peaks of C=O of methacrylate groups.

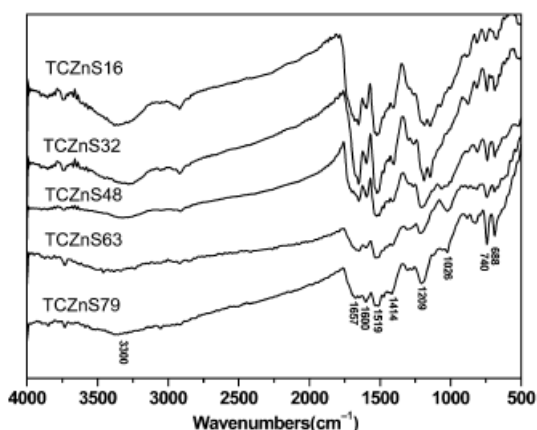


Fig. 8. FTIR spectra of nanocomposite films of TCZnS16–TCZnS79.

The CLO band gradually decreases in intensity with increasing TCZnS nanoparticles, compared with the intensity of the characteristic absorption band of phenyl (688–740 and 1600 cm^{-1}). This result indicates that an increasing amount of TCZnS with high phenyl content is immobilized into the PUMM matrix. The IR absorbances of the CLC double bonds at 1629–1639 cm^{-1} for the methacrylate groups and the capping agent (TMSt) disappear, indicating that they have completely polymerized. Fig. 9 illustrates TGA curves of pure PUMM, TCZnS16, TCZnS48 and TCZnS86 films at a heating rate of 10 $^{\circ}\text{C min}^{-1}$ under nitrogen atmosphere from 50 to 750 $^{\circ}\text{C}$.

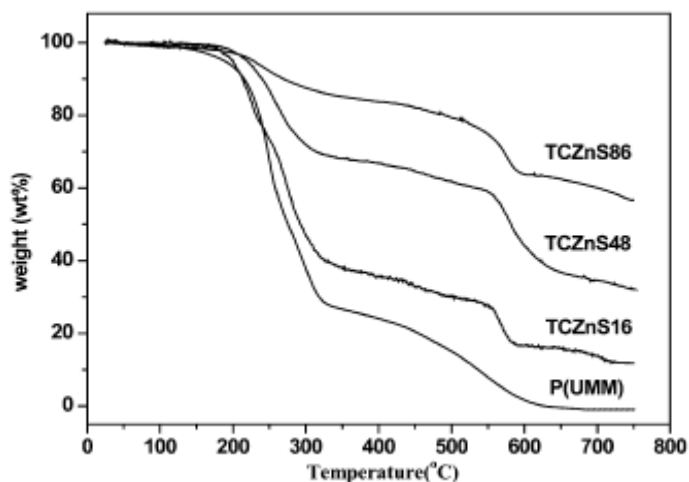


Fig. 9. TGA curves of nanocomposite films of TCZnS16, TCZnS48 and TCZnS86 at a heating rate of 10 $^{\circ}\text{C min}^{-1}$ under nitrogen flow.

The nanocomposite films have the initial decomposition temperatures of 201, 204 and 203 $^{\circ}\text{C}$ for TCZnS16, TCZnS48 and TCZnS86 respectively, and these values relate to the decomposition temperature of the polymer matrix (PUMM). There are two obvious weight loss regions: between 200 and 330 $^{\circ}\text{C}$, and from 550 to 600 $^{\circ}\text{C}$. The weight loss between 200 and 330 $^{\circ}\text{C}$ is predominantly attributed to the weight loss of the polymer matrix. The secondary weight loss at 550–600 $^{\circ}\text{C}$ is considered to be the weight loss of another part of the polymer and the thermal decay of the partial thiol-capped agents on the surface of ZnS nanoparticles. As shown in Table 1, the residues of the nanocomposite films TCZnS16–86 at 750 $^{\circ}\text{C}$ are in the range of 11.5–56.5% and they increase with increasing TCZnS content in the films. By and large, these char yields are in agreement with the theoretical weight fraction of inorganic ZnS contained in the films, indicating that the ZnS particles were successfully incorporated into the polymer matrices. This result also effectively supports the chemical analysis results for the TCZnS particles. Fig. 10 shows DSC curves of PUMM, TCZnS16, TCZnS48 and TCZnS79 films at a heating rate of 10 $^{\circ}\text{C min}^{-1}$ under nitrogen flow.

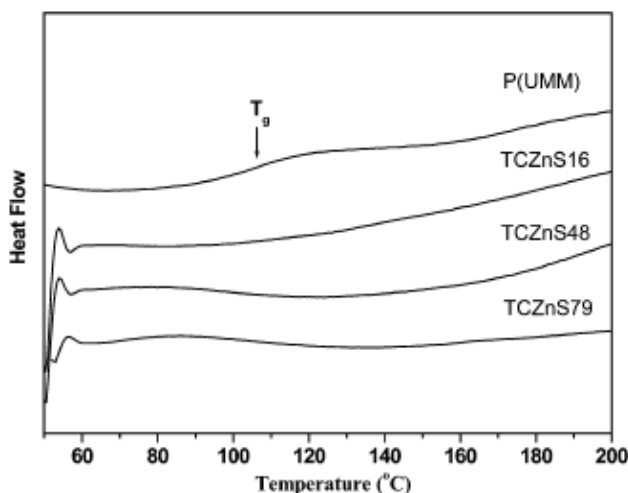


Fig. 10. DSC curves of PUMM, TCZnS16, TCZnS48 and TCZnS79 films at a heating rate of 10 °C min⁻¹ under nitrogen flow.

The pure PUMM polymer exhibits a glass transition temperature (T_g) of about 106 °C. However, no significant thermal transition peaks are observed for the ZnS-PUMM nanocomposites below 200 °C. Also was used the torsion braid analysis (TBA) to measure the thermal transition behavior of the nanocomposite samples. The T_g of the polymers still are not observed. This suggests that nanocomposites have higher rigidity and crosslinking density due to the incorporation of the thiol-capped ZnS nanoparticles, which restricted the motion of the polymer chain segments. Thus, it may be that the glass transition temperature of the polymer is close to the decomposition temperature of it. Thermal analyses indicate that the ZnS nanoparticles were successfully immobilized into the polymer matrix and the nanocomposite films exhibit a good thermal stability.

Maximal weight concentration of thiol capped ZnS is around 86% as at higher concentration nanocomposite films with good mechanical properties cannot be obtained.

Another example of ZnS and CdS high concentration nanocomposite give the work [13, 14]. In the work has involved nanoparticles stabilization primarily by steric barriers. So, each nanoparticle should be covered by quite a thick shell linked with the surface of nanoparticle. This was accomplished by having a multi-atom chain connecting the acid group and aromatic group of the shell molecule.

Was used UV curable monomers with an acid group at one end and a vinyl group at the other and low viscosity at room temperature to accomplish both bonding to nanoparticle surface and, same time, possibility to UV-curing. Based on these requirements one suitable substance has been chosen: 2-carboxyethyl acrylate (CEA). This substance has an acrylic group for curing and can be used as shell material because of the acid group. This molecule has only a short distance between the groups, and only a relatively thin shell would be expected before polymerization. And we know that a thin shell formed at synthesis of nanoparticles is not enough at high nanoparticles concentration in a thermoplastic matrix. Certainly, we would expect additional monomer units to add to the shell monomers during the UV curing reaction.

The method to introduce the ZnS nanoparticles into CEA found is the following: ZnS nanoparticles with the shell of 5-Phenylvaleric acid have been put into toluene and heated for 10 hours at 80 °C. This operation is needed to remove residue water from the nanoparticles surface. After the nanoparticles powder was dried in air at 80 °C during 10 minutes, it was put into CEA. Ultrasonic dispersion for about 30 – 40 minutes in apparatus was done.

After dissolution of ZnS into CEA, a shell of CEA is formed at the surface of each nanoparticle. As the result ZnS – CEA nanocomposite dispersion (or solution) is stable for a long time.

UV curing of nanocomposite was made by usual way by addition of photoinitiator and curing a film with UV light. Experimental conditions: photoinitiator Dimethoxy phenyl acetophenone 0,1 w%, film thickness 100 um, UV light 365 nm, 5 mW/cm², room temperature, time of curing 10 minutes. Maximal ZnS volumetric concentration in the compositions was 25%. The resulting RI of the UV cured film was 1,65, compared with an RI of 1,45 for the pure CEA film. Thus, the RI increase is 0,20. Dependence of RI on nanoparticles concentration is shown in Fig. 11 Maximal nanoparticles concentration has been limited by viscosity increase up to the point of a non-flowing composition.

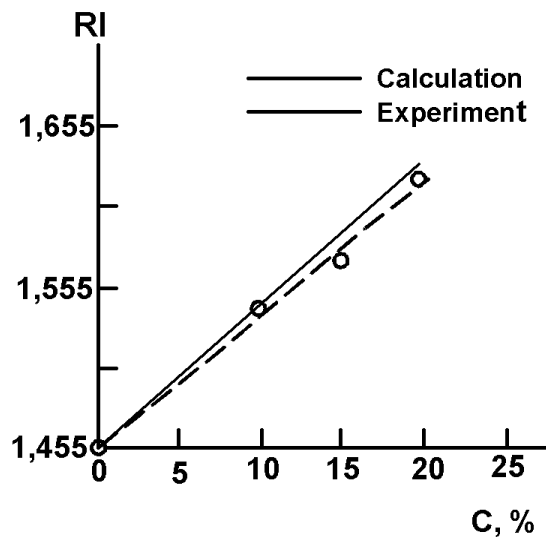


Fig. 11. Dependence of nanocomposite RI on nanoparticles concentration.

TEM photo (Fig 12) shows inside structure of nanocomposite. The photo was made of a nanocomposite cured immediately after preparation. The nanoparticles concentration is 20 vol.%. Note that the distribution of particles is almost uniform, which explains the transparency.

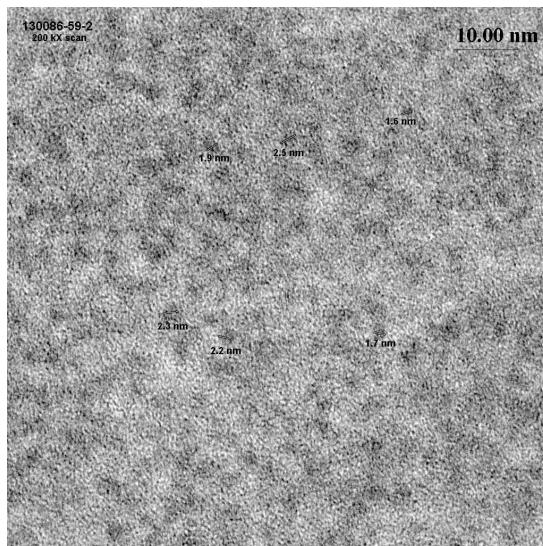


Fig. 12. TEM photo of ZnS-CEA nanocomposite (nanoparticles concentration is 20 vol. %)

4. Electron and hole transport over disperse nanocomposite systems and nanolayers

At present time charge transport over disperse semiconductor were investigated mostly for organic conjugated materials. For high concentration nanocomposite materials are used same understanding. In this chapter will be considered charge transport over disperse organic materials as the nearest analog of nanocomposite.

At organic materials when atoms are bonded together to form a molecule, the upper atomic orbitals interact with each other to form delocalized molecular orbitals while the deep atomic orbitals are still localized in the atomic potential well (Fig. 13 a) [15].

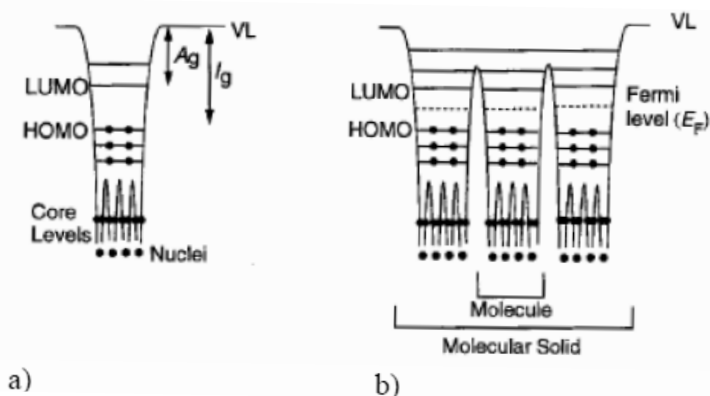


Fig. 13. Electronic structures of (a) a polyatomic organic molecule or a single chain polymer and (b) an organic solid.

When the orbital overlap occurs directly between the nuclei of the atoms, the orbitals form σ -bond and the sideways overlapping of the orbitals form π -bonds. Materials having π -bonds orbitals are named as conjugated materials same time. It is the π electrons which mainly determine the electronic and optical properties of the molecule. In ground state, the π -electrons form the π -band and the highest energy π -electron level is known as the highest occupied molecular orbital (HOMO). In excited state, the π -electrons form the π -band and the lowest energy π -electron level is known as the lowest unoccupied molecular orbital (LUMO). The HOMO resembles the valence band and the LUMO resembles the conduction band in the inorganic semiconductor concepts. The energy separation between the HOMO and the vacuum level corresponds to the gas phase ionization energy (I_g) and that between the LUMO and the vacuum level corresponds to the gas phase electron affinity (A_g) [2.1]. In an organic solid, the molecules or polymer chains are packed closely together and result in an electronic structure as shown in Figure 13b. It can be observed that the electronic states are localized to individual molecules with narrow intermolecular band widths.

4.1 Excitons in organic

When an electron has been excited from the ground state orbital to a higher orbital, it leaves a hole in the ground state orbital. The resulting bound state of an electron and a hole due to the Coulombic interaction is called an exciton. In general, excitons can be divided into two classes. If it is delocalized with radius much larger than the interatomic spacing, it is a Mott-Wannier type of exciton. On the other hand, if it is localized and tightly bound, it is called a Frenkel exciton. In organic materials, since the excitations are often localized on either individual molecules or a few monomeric units of a polymer chain, the excitons are highly localized and are considered to be Frenkel excitons which usually have large binding energy of some tenths of an eV or even higher. For example, in the case of Alq₃, a commonly used OLED material, the exciton binding energy is ~ 1.4 eV.

4.2 Transport

According statement in beginning of this paragraph, properties of disperse systems will be considered in example of conjugated polymers charge transport theory and abbreviation of polymer semiconductor is suitable for other disperse systems included nanoparticles in polymer matrix. According to this in mostly part of recent works nanoparticles like fullerene C₆₀ are investigated with large organic molecules like phthalocyanine and perylen together as component of polymeric disperse compositions.[16]

Electronic properties of polymers can be described in terms of semiconductor physics [17]. The particular framework of one dimensional periodic media is well suited to the basic understanding of an isolated polymer chain [18]. Polymers are bonded by strong covalent bonds. As π -orbitals overlap is weaker than s -orbitals overlap, the energy spacing (band gap) between bounding and antibounding molecular orbitals is larger for the π - π^* difference than for the σ - σ^* one. One can thus, in a first approach, limit the band study to the π - π^* molecular orbitals. Those are respectively the HOMO (for Highest Occupied Molecular Orbital) and LUMO (for Lowest Unoccupied Molecular Orbital), in terms of molecular physics. They are also the usual valance (VB) and conduction bands (CB) of

semiconductor physics, respectively σ -bonds then only contribute to the stability of the molecular structure.

In a real material also, 3-dimensional interactions play a major role in transport properties, even dominating the transport which becomes an interchain hopping process. Small molecules are bounded by weak interactions in the condensed state: Van der Waals forces. There results a weak coupling between them, the resonance integral t_1 is thus small (tenth of eV at most) [19], resulting in narrow flat bands. Mobility is thus a priori smaller in small molecules, owing to a large effective mass

$$m^* = \frac{n^2}{2} \left(\frac{\partial^2 E}{\partial k^2} \right)^{-1}$$

There can of course be exceptions to such a rule, the interdistance spacing can be small and molecular materials can in fact possess a rather large mobility. The first electrically pumped injection organic laser was indeed made from small molecules (a tetracene single crystal) [20].

Transport and mobility in organic materials require a knowledge of the charged species. A review of transport properties is given by Schott [21]. Energy levels of the charges are usually determined by cyclic voltametry for materials in solution. They can be characterized by XPS or UPS (X-ray and UV photoelectron spectroscopies) for solid materials. In small molecules, charged species are localized spatially, they are simply the cation (positive) and anion (negative) radicals. In polymers, the electron-phonon coupling leads to the so-called polarons which are charges dressed by a reorganization of the lattice [22]. Polarons may be regarded as defects in conjugated polymer chains. Such defect stabilises the charge which is thus self-trapped as a consequence of lattice deformation. So in the vast majority of organic semiconductors, transport bears all characteristics of a hopping process in which the charge (cation or anion) propagates via side to side oxidation-reduction reactions (Fig. 14.).

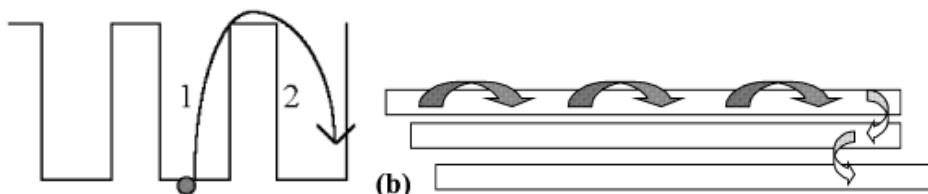


Fig. 14. Hopping process between molecules 1 and 2. b- Intra- (full arrows) and intermolecular (broken arrows) charge-transport.

One must distinguish between intramolecular charge transport along a conjugated polymer chain and intermolecular charge transport between adjacent molecules or polymer chains (Fig. 14 b.).

The former which is specific to conjugated polymers is the most efficient. Charge mobility in organics is field dependent, especially in the low mobility materials in which it usually follows phenomenologically a Poole-Frenkel law: $\mu\alpha \exp(\sqrt{E})$ [23]. Mobility can be

Thank You for previewing this eBook

You can read the full version of this eBook in different formats:

- HTML (Free /Available to everyone)
- PDF / TXT (Available to V.I.P. members. Free Standard members can access up to 5 PDF/TXT eBooks per month each month)
- Epub & Mobipocket (Exclusive to V.I.P. members)

To download this full book, simply select the format you desire below

